A&A, 683, A237 (2024)
https://doi.org/10.1051/0004-6361/202348187

Astronomy & Astrophysics

Type Ia supernovae from chemically segregated white dwarfs

E. Bravo[1], J. Isern[2,3,4], and L. Piersanti[5,6]

[1] Departamento de Física Teórica y del Cosmos, Universidad de Granada, 18071 Granada, Spain
e-mail: eduardo.bravo@ugr.es
[2] Institut de Ciències de l'Espai (ICE, CSIC), Campus UAB, C/ de Can Magrans s/n, 08193 Cerdanyola del Vallès, Spain
[3] Institut d'Estudis Espacials de Catalunya (IEEC), C/ Gran Capità 2-4, 08034 Barcelona, Spain
[4] Observatori Fabra, Mathematics and Astronomy Section (RACAB), Rambla dels Estudis 115, planta 1a, 08002 Barcelona, Spain
[5] INAF – Osservatorio Astronomico d'Abruzzo, via Mentore Maggini, snc, 64100 Teramo, Italy
[6] INFN – Sezione di Perugia, via Pascoli, Perugia, Italy

Received 6 October 2023 / Accepted 16 January 2024

ABSTRACT

Type Ia supernovae are the outcome of the explosion of a carbon–oxygen white dwarf in a close binary system. They are thought to be the main contributors to the galactic nucleosynthesis of iron-peak elements, with important contributions to the yields of intermediate-mass elements. Recent analyses of the phase diagram of carbon and oxygen containing impurities such as ^{22}Ne and ^{56}Fe in conditions relevant to white dwarf interiors suggest that both isotopes can partially separate when the temperature of the star is low enough to start solidifying. The purpose of the present paper is to examine the impact of this separation on the yields of the different chemical species synthesized during explosions. We used a one-dimensional supernova code to evaluate the impact of the sedimentation assuming different degrees of chemical separation. We find that the main properties of the ejecta, the kinetic energy, and the ejected mass of ^{56}Ni only vary slightly when the separation is taken into account. However, the yields of important isotopes that are used as diagnostic tools, such as manganese, can be strongly modified. Furthermore, the chemical separation studied here is able to change several indicators related to the metallicity of the progenitor (such as the mass ratio of calcium to sulphur in the ejecta or the UV flux of the supernova) and to its mass, whether it is a Chandrasekhar-mass white dwarf or a substantially lighter one (such as the imprint of stable nickel on late-time infrared spectra or that related to the presence of radioactive nickel at the center of the ejecta).

Key words. nuclear reactions, nucleosynthesis, abundances – supernovae: general – white dwarfs

1. Introduction

Type Ia supernovae (SNe Ia) are the outcome of the explosion of a carbon–oxygen (CO) white dwarf (WD) in a binary system. They are thought to be the main contributors to the nucleosynthesis of the galactic iron peak elements, and important inputs to the synthesis of intermediate-mass isotopes; although other sources, such as core-collapse supernovae, also contribute.

Observations of SN 2014J obtained with INTEGRAL in the γ-ray domain proved that the light curves of SNe Ia are powered by the radioactive decay of ^{56}Ni (Churazov et al. 2014, 2015; Diehl et al. 2014; Isern et al. 2016), while near-infrared observations of the innermost regions of SN 2011fe during the nebular phase revealed the presence of important amounts of stable iron-group species such as ^{54}Fe and ^{58}Ni (Mazzali et al. 2015), implying an important degree of neutronization. This excess of neutrons comes partially from the presence of neutron-rich species inherited from the progenitor of the WD and partially from the electron captures before and during the explosive phase in those regions where density is higher than $\sim 10^9$ g cm^{-3}. If the resulting neutron excess is high enough, nuclear statistical equilibrium (NSE) matter is no longer dominated by radioactive ^{56}Ni but by stable ^{54}Fe and ^{58}Ni or by species that are neutronized to an even greater degree.

The outcome of such explosions depends on the abundance and distribution of the different chemical species, the mass and physical state of the WD, and the ignition mode and the characteristics of the burning front. The scenarios that have been proposed to trigger the explosion can be roughly outlined as follows:

– Single degenerate (SD): This scenario assumes that a CO WD accretes matter from a nondegenerate companion, which can be a main sequence star, a red giant star (Whelan & Iben 1973; Nomoto 1982b; Hachisu et al. 1999; Han & Podsiadlowski 2004), or a helium star, and explodes when it reaches the Chandrasekhar's mass or when the accreted helium layer reaches a critical thickness (Nomoto 1982a; Woosley & Weaver 1994; Livne & Arnett 1995).
– Double degenerate (DD): This scenario assumes two stars in sufficient proximity to experience two episodes of common envelope evolution that lead to the formation of two WDs. If the final separation is $\lesssim 1\,R_\odot$, the system loses angular momentum via emission of gravitational waves at a rate that allows them to merge in less than a Hubble time (Iben & Tutukov 1984; Webbink 1984).
– White dwarf–white dwarf collision (WDWD): In this scenario it is assumed that two WDs collide and immediately ignite (Rosswog et al. 2009; Lorén-Aguilar et al. 2010). This collision can be caused by a fortuitous encounter in a dense environment, for instance the core of a globular cluster or the central regions of a galaxy, or by the interaction of a binary WD in a hierarchical triple or quadruple system via the Kozai-Lidov mechanism (Kushnir et al. 2013; Fang et al. 2018; Hamers & Thompson 2019).

All these scenarios share a commonality in that the time elapsed from the birth to the start of accretion and to the explosion of

the WD can be very different depending on the parameters of the binary system. During this time, the WD experiences chemical evolution caused by the gravitational diffusion of neutronized species and by stratification due to crystallization, which can modify the ignition density, the velocity of the burning front, and the number of electron captures.

White dwarfs with an initial mass of $\lesssim 1.05\,M_\odot$ are made of a mixture of ^{12}C and ^{16}O with an abundance distribution that depends on the mass and metallicity of the progenitor (Salaris et al. 1997). In addition to these two isotopes, the WD contains ^{22}Ne and other isotopes inherited from the progenitor according to its initial metallicity. In particular, ^{22}Ne is the result of the α-burning of the ^{14}N left over from the hydrogen burning stage and its abundance is of the order of the sum of the initial carbon, nitrogen, and oxygen abundances; e.g., $X(^{22}\mathrm{Ne}) \sim 0.02$ for solar metallicities.

During the fluid phase, matter is composed of a mixture of carbon, oxygen, and neon (CONe) (Ogata et al. 1993) and the chemical evolution of the star is dominated by the gravitational diffusion of the existing heavier isotopes, with ^{22}Ne being the most important reservoir of neutrons (Bravo et al. 1992; Bildsten & Hall 2001; Deloye & Bildsten 2002). Self-consistent calculations showed that ^{22}Ne is effectively depleted in the outermost layers and that this mechanism is only efficient in massive WDs (i.e., $M \gtrsim 1\,M_\odot$; García-Berro et al. 2008; Althaus et al. 2010; Camisassa et al. 2016) in agreement with the earlier guess by Bravo et al. (1992).

During the process of solidification, Coulomb plasmas experience a change of miscibility and, as a consequence, the chemical profile of the stars is modified. It is commonly accepted at present that the phase diagram of solidifying CO binary mixtures has an azeotropic composition at $x_\mathrm{O} \approx 0.2$, where x_O is the abundance of oxygen by number (Ichimaru et al. 1988; Ogata et al. 1993; Horowitz et al. 2010; Medin & Cumming 2010; Blouin et al. 2020). As the abundance of oxygen in the major part of the star is higher than the azeotropic value, the solid mixture in equilibrium with the liquid is enriched in oxygen and, being denser, sinks towards the inner regions of the WD. The final outcome is an oxygen enrichment of the inner layers and a depletion in the outer layers (Mochkovitch 1983; Hernanz et al. 1994; Segretain et al. 1994; Isern et al. 1997, 1998, 2000; Renedo et al. 2010; Salaris et al. 2010; Blouin et al. 2020).

The distribution of trace chemical species with a neutron excess, such as ^{22}Ne and ^{56}Fe, can also be modified by the process of crystallization (Isern et al. 1991; Xu & van Horn 1992). Although the calculation of the phase diagram for Coulomb binary mixtures appears to be settled, that is, as far as quantum effects are not relevant, the case of impurities is still posing important problems (Saumon et al. 2022).

In the first attempt to guess the behavior of ^{22}Ne (Isern et al. 1991), it was assumed that it was possible to approach the CONe ternary mixture as a binary one consisting of neon and an average isotope with atomic number $\langle Z\rangle = 6x_\mathrm{C} + 8x_\mathrm{O}$, with x_C being the fraction number of carbon. Under this hypothesis, the authors found an azeotrope for a neon abundance in the range of 0.05–0.09 by mass. As the abundance of neon is expected to be lower than this value, the resulting solid is poorer in neon and – being lighter than the liquid – floats and mixes with the ambient, which is the so-called distillation process (Mochkovitch 1983), and leads to the formation of a core with the azeotropic composition and containing all the neon of the star and producing an important release of gravitational energy (Isern et al. 1991). Later on, assuming the same hypothesis of averaging the CO mixture, Segretain et al. (1994) obtained an azeotropic behavior at $x_\mathrm{Ne} = 0.13$ by number.

The hypothesis of an average nucleus is doubtful, at least for species with nearby atomic numbers, as shown by Segretain (1996). This latter author found that, if the abundance of oxygen is high, the presence of neon is irrelevant and the phase diagram is similar to a pure CO one. He also found the existence of an azeotropic point with $x_\mathrm{Ne} = 0.22$, $x_\mathrm{C} = 0.78$, and $x_\mathrm{O} = 0.0$ that allowed the formation of a carbon–neon shell without oxygen. Recently, Blouin et al. (2021, see their Fig. 3) also found that, depending on the relative abundance of oxygen, it is possible to obtain stars with a neon-rich core or a carbon–neon shell without oxygen. More precisely, depending on the initial WD composition, these authors found three possible configurations: (a) If the liquid is rich enough in ^{22}Ne, the solid in equilibrium is poor in neon, crystals float, and the final outcome is a solid core with a composition $(x_\mathrm{C}, x_\mathrm{O}, x_\mathrm{Ne}) = (0.8, 0.0, 0.2)$ by number surrounded by a CO mantle free of neon that crystallizes as usual. (b) If the central mixture is oxygen poor, the distillation process can proceed and the final outcome is a neon-rich core surrounded by a CO mantle as in case (a). Finally, (c) if the composition is approximately standard, with $x_\mathrm{O} = 0.53$, $x_\mathrm{Ne} = 0.009$ for instance, the distillation process cannot start and the solid has the composition predicted by the CO mixture without changes in the neon distribution. However, as the outer layers are gradually depleted in oxygen, there is a moment at which the distillation starts and the final outcome is a CONe core surrounded by a carbon–neon (CNe) shell, itself surrounded by a CO mantle free of neon.

The sedimentation of ^{56}Fe can also play an important role (Xu & van Horn 1992). Segretain et al. (1994), within the hypothesis of an effective binary mixture, found a eutectic behavior and, as the abundance of this impurity is lower than the eutectic value, the outcome is a distillation process that creates an iron-rich core at the center. This case was recently examined by Caplan et al. (2021), who found that Fe-rich crystals separate before solidification of the rest of the mixture and create an iron-rich core that can be made of nearly pure iron or a carbon–oxygen–iron (COFe) alloy, depending on the exact composition of the star. As this phenomenon occurs very early, concentric shells containing different impurities can form, such as an Fe-rich core surrounded by a Ne-rich shell and both surrounded by a CO mantle.

Recently, Keegans et al. (2023) computed the yields for a wide set of uniformly distributed ^{22}Ne abundances in a $1.4\,M_\odot$ delayed detonation, and 1.0 and 0.8 double-detonation cases. These authors find that the influence is negligible for mass fractions of neon of below $\lesssim 10^{-4}$ but not for abundances of $\gtrsim 10^{-3}$. In any case, the resulting yields have to be examined isotope by isotope.

A question that arises in this respect refers to what happens in the case where neon and iron are not uniformly distributed because they migrate towards the central regions. This question is relevant because, depending on the system considered, the white dwarf can start to crystallize before starting the accretion process and, if this is the case, the explosion will develop within a completely different chemical structure.

The first attempt to analyze the impact of ^{22}Ne distribution on SNe Ia nucleosynthesis[1] was made by Bravo et al. (1992), who found that if this isotope is placed at the center, its

[1] By this epoch, the problem was the excess of ^{54}Fe and ^{58}Ni predicted by the W7 model, the most popular theoretical model of SNe Ia (Nomoto et al. 1984).

contribution to the neutron excess is negligible, thus alleviating the problem.

The impact of gravitational diffusion of ^{22}Ne and sedimentation of the CO mixture – but excluding the distillation of ^{22}Ne – on the SNe Ia yields was examined by Bravo et al. (2011) in the Chandrasekhar and sub-Chandrasekhar scenarios, assuming spherical symmetry and neglecting convective mixing during the simmering phase. These authors found a negligible influence on the supernova properties, except on those depending on the ignition density and propagation of the flame. We must emphasize that the central abundance of ^{22}Ne assumed in this latter study is much lower than its azeotropic value.

The consequences of disrupting a WD containing a pure ^{12}C–^{22}Ne layer in a WDWD collision were analyzed by (Isern & Bravo 2018a,b), who found that part of this shell could survive, therefore providing an alternative explanation to the long-lasting problem of the origin of the meteoritic Ne–E anomaly.

The time necessary to start solidification depends on the mass of the white dwarf, because the crystallization temperature depends on density, $T_s \propto \rho^{1/3}$, and on the detailed chemical composition. Furthermore, this time also depends on the nature of the outer envelope of the white dwarf; those with a H-layer (i.e., of spectral type DA) cool more slowly than those lacking one (non-DAs). Typical cooling times necessary to begin crystallization are in the range of 0.2–6 Gyr, when the mass of the white dwarf goes from 1.2 to 0.4 $M_\odot$. The typical delay time for the explosion in the SD case is in the range of 0–1 Gyr, while in the DD case this delay is in the 1–10 Gyr range, with a decaying rate $\propto t^{-1}$ (Han et al. 2008; Maoz et al. 2012). The typical accretion rates in the first case are in the range of 10^{-8}–10^{-7} $M_\odot$ yr^{-1}, and this is how the cooling times can be sufficient to allow (at least) partial crystallization. In the DD case, the cooling time can be arbitrarily long, as is true in the case of collisions. Here, the casuistry is very large, because it depends on the binary systems considered. As the goal of this study is to explore the influence of chemical sedimentation, only the extreme cases were considered.

In the following section, we report the methods used in this study. In Sect. 3, we present our analysis of the consequences of the sedimentation of ^{22}Ne for the outcome of a SNe Ia explosion, while in Sect. 4 we consider the consequences of bringing ^{56}Fe to the central regions of the star. Section 5 is devoted to the explosion of a WD where both isotopes ^{56}Fe and ^{22}Ne have migrated to the center. Finally, in Sect. 6, we present the conclusions of the present work.

2. Methods

In this work, the thermonuclear supernova explosion of a WD is simulated using the one-dimensional hydrodynamic code described in detail in Bravo et al. (2019). The WD is initially in hydrostatic equilibrium and is isothermal; its chemical composition is described in the following sections. The code integrates the hydrodynamic evolution using a large nuclear network including 722 isotopes (the same as in Bravo & Martínez-Pinedo 2012, where details can be found) and several thousand nuclear reactions[2]. It solves the Saha equations for NSE when applicable, and calculates the neutronization rate and associated neutrino energy losses at each time step, computing the weak interaction rates on the NSE composition. The rate of the fusion reaction ^{12}C+^{16}O is that recommended in Caughlan & Fowler (1988).

Concerning the explosion mechanisms, two possibilities are considered here: a detonation of a bare CO sub-Chandrasekhar-mass structure, and a delayed detonation of a Chandrasekhar-mass CO WD. In the massive WD models, the rehomogenization by convection during simmering is not taken into account, as justified in Sect. 3.2.

3. ^{22}Ne sedimentation: Scenarios and models

Following Blouin et al. (2021), we considered two different scenarios for the chemical distribution of ^{22}Ne after freezing: a central enhancement of the abundance of ^{22}Ne, if the WD metallicity is sufficiently high ($Z = 0.035$), cases A and B in Fig. 1; and an off-center shell heavily enriched in the same isotope containing carbon and depleted of oxygen, if the initial WD metallicity is not sufficiently high ($Z = 0.014$), case C in Fig. 1. Evidently, the number of different chemical structures can be very large, but these cases provide the framework necessary to analyze the impact of the chemical structure of the exploding WD at thermonuclear runaway.

In case B, referred to below as "full", all the ^{22}Ne initially present in the WD is located in a central sphere with the azeotropic mass fraction $X(^{22}\mathrm{Ne}) = 0.30$ and $X(^{12}\mathrm{C}) = 0.70$, that is the oxygen nuclei have been expelled from the center of the WD. For a WD of mass 1.06 $M_\odot$, the full process of separation of ^{22}Ne may last of the order of 7–9 Gyr (Blouin et al. 2021). Therefore, it is possible that the instability leading to a SNe Ia explosion occurs in the middle of the sedimentation process. This option is represented by case A, later referred to as "half", in which only half of ^{22}Ne nuclei have had time to settle in the central region, while the other half remains disseminated throughout the rest of the WD with an abundance of $X(^{22}\mathrm{Ne}) = 0.0187$.

Case C, later referred to as "shell", holds when the initial oxygen abundance is relatively high; here it is assumed to be $X(^{16}\mathrm{O}) = 0.6$. First, an oxygen-rich and carbon-poor solid forms and migrates towards the innermost regions of the WD[3]. In this process, the regions of the WD external to the solidified ball become enriched in carbon. When the mass fraction of carbon in these regions reaches the azeotropic abundance, $X(^{12}\mathrm{C}) = 0.70$, a shell starts forming in which there is only carbon and ^{22}Ne, with $X(^{22}\mathrm{Ne}) = 0.30$. The formation of the ^{22}Ne-rich shell takes a relatively short time, of the order of a couple of gigayears (Blouin et al. 2021). Finally, when all the remaining ^{22}Ne is packed in the shell, the WD is wrapped by an envelope made of carbon and oxygen. The mass coordinates of the different elements of such a chemical structure, normalized by the total WD mass, are determined by the phase diagram and the initial abundance of each isotope.

The list of explosion models is given in Table 1, where $M_{\rm WD}$ is the mass of the WD, ρ_c its central density, Z is the progenitor metallicity – equal to the overall abundance of ^{22}Ne in the WD – and $X(^{16}\mathrm{O})$ is the abundance of ^{16}O. The radial profile of the distribution of ^{22}Ne is given as $^{22}\mathrm{Ne}_{\rm core}$: it may be either uniform, half, full, or shell. The uniform case, in which the chemical composition of the WD is homogeneous, is the reference for comparisons with heterogeneous models. The main result of the explosion is that the kinetic energy, K, and the ejected mass

[2] All reaction rates are taken from the JINA REACLIB compilation, namely the version from November 6, 2008: http://groups.nscl.msu.edu/jina/reaclib/db/ (Cyburt et al. 2010).

[3] According to the phase diagrams of Segretain et al. (1994) and Blouin et al. (2020), the solid starts to form when the oxygen abundance grows from 0.60 to $X(^{16}\mathrm{O}) = 0.72$.

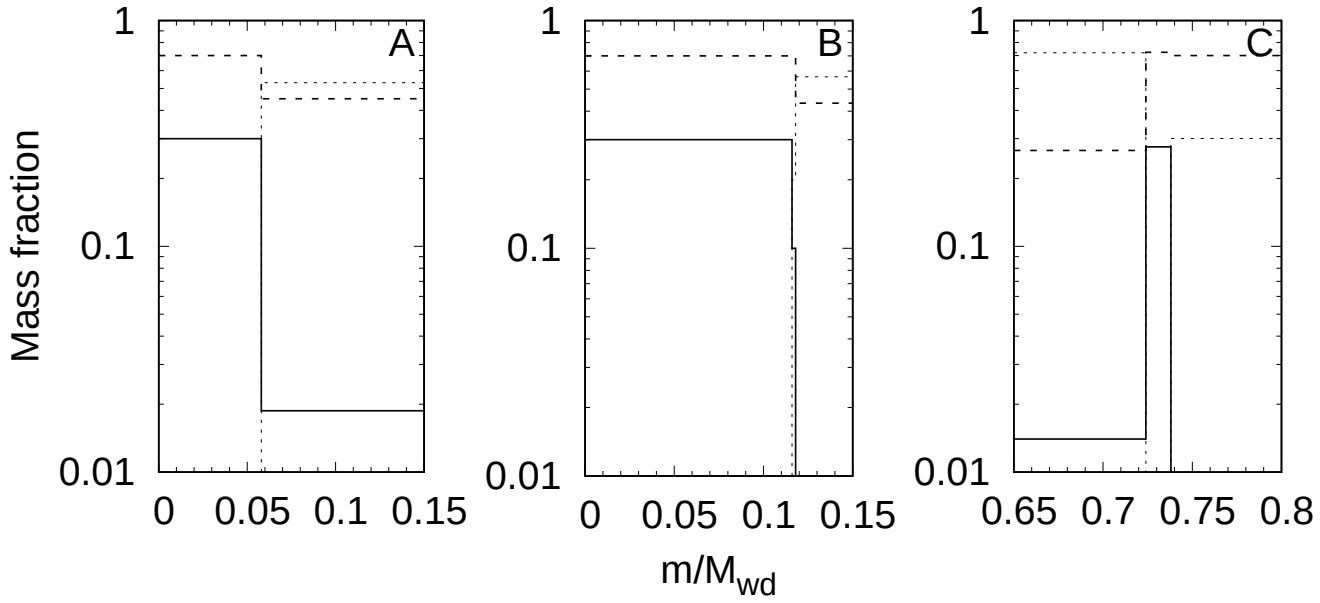

Fig. 1. Details of the different enhancements on the abundance of ^{22}Ne (solid lines) and the corresponding abundances of ^{12}C (long-dashed lines) and ^{16}O (short-dashed lines) in the models reported in Table 1. Case A or "half" (left panel): half of all ^{22}Ne concentrated in a central ball with the azeotropic composition and the other half uniformly distributed through the rest of the WD. Case B or "full" (central panel): all ^{22}Ne concentrated in a central ball with the azeotropic composition. Case C or "shell" (right panel): oxygen-rich inner region with $X(^{22}\mathrm{Ne}) = Z$, followed by a narrow shell rich in ^{22}Ne and depleted of oxygen, and then a CO envelope with no ^{22}Ne.

Table 1. Summary of WD models with different distributions of ^{22}Ne.

$M_{\rm WD}$ ($M_\odot$)	$\rho_{\rm c}$ (g·cm^{-3})	Z	^{22}Ne$_{\rm core}$ [(a)]	$X(^{16}\mathrm{O})$	K (10^{51} ergs)	$M(^{56}\mathrm{Ni})$ ($M_\odot$)	$M(^{55}\mathrm{Mn})$ ($10^{-2}\,M_\odot$)	$M(^{58}\mathrm{Ni})$ ($10^{-2}\,M_\odot$)
Bare C-O WD detonations								
1.06	5.4×10^7	0.035	Uniform [(b)]	0.50	1.331	0.652	0.597	3.94
1.06	5.7×10^7	0.035	Half [(c)]	0.50	1.328	0.641	0.548	4.70
1.06	5.9×10^7	0.035	Full [(d)]	0.50	1.330	0.635	0.238	6.36
1.06	5.3×10^7	0.014	Uniform [(b)]	0.60	1.266	0.678	0.390	1.29
1.06	5.3×10^7	0.014	Shell [(e)]	0.60	1.285	0.682	0.382	1.30
Chandrasekhar-mass WD delayed detonations								
1.38	5.0×10^9	0.035	Uniform [(b)]	0.50	1.382	0.601	1.58	3.78
1.37	5.0×10^9	0.035	Half [(c)]	0.50	1.369	0.629	1.22	2.56
1.37	5.0×10^9	0.035	Full [(d)]	0.50	1.355	0.625	0.407	2.78
1.38	6.9×10^9	0.035	Full [(f)]	0.50	1.338	0.629	0.414	1.95
1.38	5.0×10^9	0.014	Uniform [(b)]	0.60	1.283	0.603	1.12	2.71
1.38	5.0×10^9	0.014	Shell [(e)]	0.60	1.287	0.540	1.05	2.73

Notes. [(a)]Degree of concentration of ^{22}Ne in a central core with azeotropic abundance, $X(^{22}\mathrm{Ne}) = 0.30$. [(b)]Uniform composition through the whole WD, with $X(^{22}\mathrm{Ne}) = Z$ and $X(^{12}\mathrm{C}) = 1 - X(^{22}\mathrm{Ne}) - X(^{16}\mathrm{O})$. [(c)]Half of all ^{22}Ne concentrated in a central ball with the azeotropic composition; the other half uniformly distributed through the rest of the WD (case A in Fig. 1). [(d)]All ^{22}Ne concentrated in a central ball with the azeotropic composition (case B in Fig. 1). [(e)]Enhanced ^{22}Ne abundance in a narrow off-center shell (case C in Fig. 1). [(f)]Same as case B in Fig. 1 but with the same mass as the WD with uniform composition.

of ^{56}Ni, $M(^{56}\mathrm{Ni})$, are almost independent of the distribution of ^{22}Ne, while the ejected masses of ^{55}Mn and ^{58}Ni strongly depend on the chemical structure. These data are given at a time of 100 s after thermal runaway.

3.1. Bare CO WD detonation

In this section, we show the results of the explosion of a sub-Chandrasekhar-mass WD with the different distributions of ^{22}Ne outlined above. The WD mass is 1.06 $M_\odot$ and the helium cap responsible for the instability leading to a central detonation is left out of the computation (Sim et al. 2010). Once a detonation is initiated in the helium layer, a detonation may be started in the CO core either directly at the interface with the helium envelope or by convergence of an inward moving shock wave near the center of the WD. A detonation is obtained in one-dimensional simulations with a central carbon mass fraction similar to or even lower than that assumed here (e.g., Woosley & Kasen 2011). In

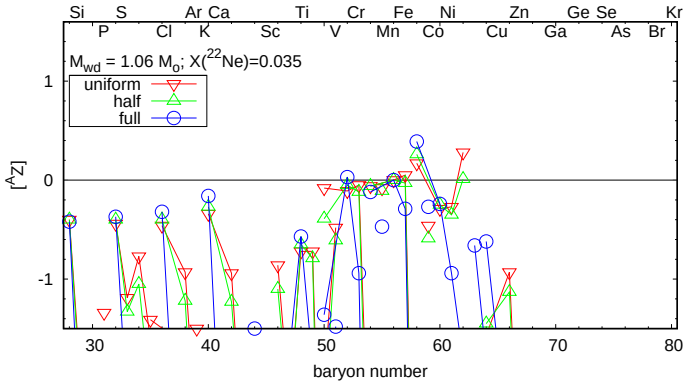

Fig. 2. Nucleosynthesis of sub-Chandrasekhar-mass bare CO models with $M_{\rm WD} = 1.06\,M_\odot$ and $Z = 0.035$ with different distributions of ^{22}Ne. The abundance of each isotope is given with reference to ^{56}Fe and normalized to Solar System abundances: $\left[{}^{A}Z\right] = \log_{10}\left[X\left({}^{A}Z\right)/X\left({}^{56}\mathrm{Fe}\right)\right] - \log_{10}\left[X\left({}^{A}Z\right)/X\left({}^{56}\mathrm{Fe}\right)\right]_\odot$, where X stands for mass fraction. All the unstable species have been allowed to decay to their stable isobars.

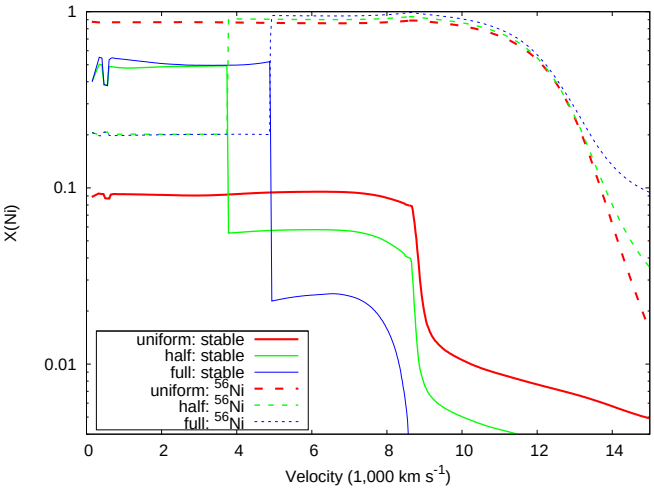

Fig. 3. Profile of ^{56}Ni and stable nickel in the inner regions of the ejecta of the models with $M_{\rm WD} = 1.06\,M_\odot$ and $Z = 0.035$ with different distributions of ^{22}Ne (see Table 1 for details). The maximum velocity shown in the plot belongs to a Lagrangian mass coordinate ~0.91 $M_\odot$.

the present work, the hydrodynamic simulation begins with the central detonation of carbon.

3.1.1. Central enhancement of the ^{22}Ne abundance

Figure 2 shows the nucleosynthesis output of the explosion of sub-Chandrasekhar-mass bare CO models with $M_{\rm WD} = 1.06\,M_\odot$ and $Z = 0.035$ with different distributions of ^{22}Ne. Only a few underproduced isotopes (with respect to ^{56}Fe and the Solar System abundances) are affected by the distribution of ^{22}Ne, where uniform and half yields are very similar, while full yields are noticeably different.

Comparing the yields of uniform and half models, the most relevant differences are as follows: ^{64}Zn and ^{66}Zn differ by ~30–40% between uniform and half models, but the abundance of the former increases after partial ^{22}Ne distillation while that of the second decreases in the same case. Also, ^{58}Ni is more abundant by ~19% in the half model, while ^{50}Cr and ^{62}Ni decrease by ~50% in the same model.

With respect to uniform versus full models, the most relevant differences after complete ^{22}Ne distillation are: increments of ^{63}Cu by a factor 51, of ^{64}Zn by a factor 9, of ^{59}Co by ~50%, and of ^{58}Ni by ~60%, and decrements of ^{62}Ni and ^{66}Zn by two orders of magnitude, ^{50}Cr and ^{53}Cr by factors 20 and 8, respectively, ^{61}Ni by a factor ~5, ^{57}Fe by a factor 2, and many others by smaller amounts.

The yields of ^{55}Mn are also affected, as they decrease after complete ^{22}Ne distillation by a factor 2.5 with respect to the uniform model. ^{55}Mn is the only stable isotope of manganese, which is an important product of SNe Ia and is relevant for chemical evolution (e.g., Eitner et al. 2020), although this decrease does not change the conclusions of the cited studies.

In summary, the total or partial concentration of ^{22}Ne in the central regions of a WD favors the synthesis of cobalt and copper in a SNe Ia explosion, while it disfavors the synthesis of manganese and chromium. The sedimentation of ^{22}Ne also changes the isotopic composition of nickel. In this respect, it is interesting to note that the amount of stable nickel synthesized in a SNe Ia has been suggested to correlate with the mass of the exploding WD, providing a discriminant between a Chandrasekhar-mass progenitor and a sub-Chandrasekhar-mass one (Blondin et al. 2022). However, ^{22}Ne sedimentation can change the trend. For instance, in the full model, the yield of ^{58}Ni is 0.064 $M_\odot$, which is higher than in any of the Chandrasekhar-mass models presented in Sect. 3.2 (see also Fig. 5 and Table A.1 in Blondin et al. 2022).

It is also remarkable that there is an increase in the mass ratio of calcium with respect to sulphur of the order of 28% in the full model as compared with the uniform model, as a consequence of the disappearance of the neutron excess carried by ^{22}Ne in the layers where these species are synthesized. This effect, albeit modest in magnitude[4], may be relevant and could help with matching X-ray spectral data concerning the abundances of these elements in SNe Ia remnants (De et al. 2014; Martínez-Rodríguez et al. 2017), as it can make the explosion of a WD with a super-solar metallicity progenitor appear to be due to a low-metallicity progenitor.

Besides the nucleosynthetic outcome of SNe Ia, the redistribution of the neutron excess of the WD prior to its explosion may have some more directly observable consequences. For example, one is related to the profile of stable and radioactive nickel isotopes (Fig. 3). In contrast with the homogeneous case, in both the half and the full models, there is a high abundance of stable nickel in the layers moving slower than 4000–5000 km s^{-1}, while ^{56}Ni is absent in the same regions. In SN 2003du, for instance, the shape of infrared lines due to [Fe II] suggests that the central volume of the ejecta up to an expanding velocity of 3000 km s^{-1} is mostly made of nonradioactive iron-group isotopes, and is surrounded by a region of radioactive ^{56}Ni up to 10 000 km s^{-1} (Höflich et al. 2004). Such chemical structure has been attributed to burning at high density, as expected in Chandrasekhar-mass progenitors. However, as shown in Fig. 3, the same structure can be mimicked by a sub-Chandrasekhar-mass progenitor in which ^{22}Ne has been totally or partially concentrated in the center of the WD prior to the SN explosion.

3.1.2. Explosion after ^{22}Ne distillation in a solar metallicity WD

Figure 4 shows the final yields of the explosions with $M_{\rm WD} = 1.06\,M_\odot$, $Z = 0.014$, and different distributions of ^{22}Ne, either

[4] Martínez-Rodríguez et al. (2017) measure calcium-to-sulphur mass ratios varying as much as 69% between different SNe Ia remnants.

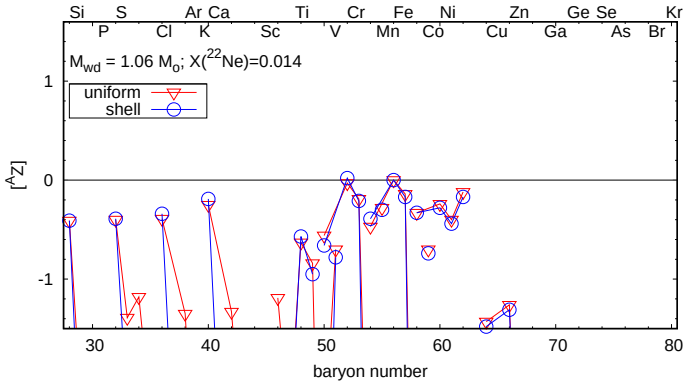

Fig. 4. Same as Fig. 2, but for the sub-Chandrasekhar-mass models with $M_{\rm WD} = 1.06\,M_\odot$ and $Z = 0.014$.

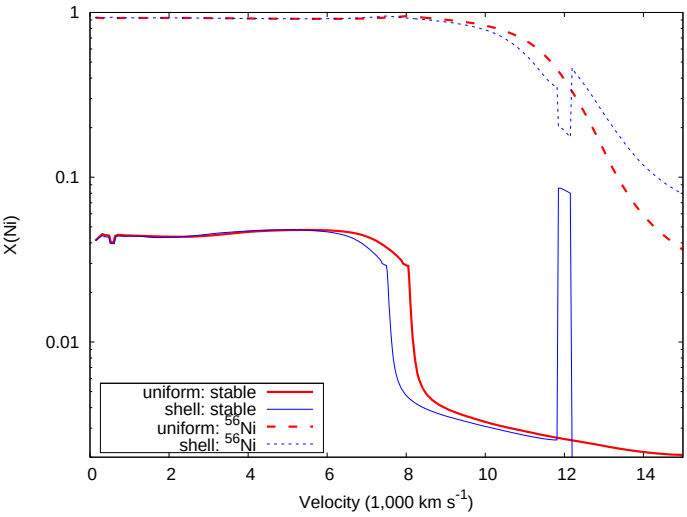

Fig. 5. Profile of ^{56}Ni and stable nickel in the inner regions of the ejecta of the models with $M_{\rm WD} = 1.06\,M_\odot$ and $Z = 0.014$ with different distributions of ^{22}Ne (see Table 1 for details).

homogeneous or an oxygen-rich core followed by a narrow off-center shell with the azeotropic composition of carbon and neon surrounded by a CO envelope (the shell model). As expected, and evidenced by Fig. 4, decreasing the progenitor metallicity reduces the effect of redistributing the ^{22}Ne through the WD. In the shell model, the most noticeable change affects ^{54}Fe, the yield of which increases with respect to the uniform model by 21%, while the final abundances of ^{40}Ca and ^{52}Cr increase by 15%. On the other hand, the yields of many neutron-rich isotopes of intermediate-mass elements decrease in the shell model; although their abundance was already quite low in the uniform model. The only isotope with a non-negligible yield in the uniform model that is negatively affected by the redistribution of neutron excess in the shell model is ^{50}Cr, the abundance of which decreases by 20%.

Figure 5 shows the profiles of the final mass fraction of stable nickel isotopes and that of ^{56}Ni (as in Fig. 3). The concentration of ^{22}Ne and, consequently, of neutron excess in an off-center shell leaves an almost imperceptible imprint but for the abundance spike of stable nickel, visible at an expansion velocity of $\sim$12 000 km s^{-1} in the shell model. Such an enhancement of nickel abundance in a narrow shell may be hard to detect in actual supernovae.

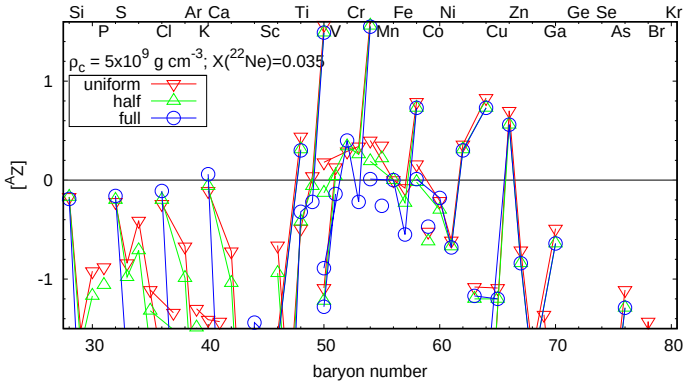

Fig. 6. Same as Fig. 2, but for the Chandrasekhar-mass models with $\rho_{\rm c} = 5 \times 10^9\,{\rm g\,cm^{-3}}$ and $Z = 0.035$.

3.2. Chandrasekhar-mass white dwarfs

In this section, it is assumed that the explosion is triggered by a delayed detonation starting as a deflagration in a Chandrasekhar-mass WD with a central density of $\rho_{\rm c} = 5 \times 10^9\,{\rm g\,cm^{-3}}$ (Piersanti et al. 2022) in the uniform and in the chemically segregated cases.

A question to address is whether or not the chemically segregated structure is able to survive the accretion and simmering phases that precede thermal runaway. The simmering phase starts when the temperature is high enough so that cooling by thermal neutrinos cannot compensate the nuclear energy release rate, and ends in thermonuclear runaway, and is characterized by an efficient convective mixing of the innermost regions of the WD. As shown by Piersanti et al. (2022), convection during the simmering phase may be restricted to the central $\sim$0.11 $M_\odot$. Therefore, the chemical structure of the initial models shown in Fig. 1 may be preserved, with the possible exception of case A; in case C, it is certainly preserved[5].

3.2.1. Central enhancement of the ^{22}Ne abundance

Figure 6 shows the nucleosynthetic results in the uniform, full, and half cases. The impact of the sedimentation of ^{22}Ne at the center of the WD is even milder than in the sub-Chandrasekhar-mass models. This is because the center of the massive WD experiences huge electron captures during the first second of the explosion, which erases most of the traces of the previous presence of a neutron excess there. When comparing the half and the uniform models, the most relevant change in the abundances affects ^{50}Cr, the yield of which is reduced in the half model by a factor two, while those of ^{54}Fe and ^{58}Ni are reduced by $\sim$35%.

On the other hand, in the full model, the only substantial yield increase with respect to the uniform model affects ^{52}Cr, whose abundance increases by 30%. By contrast, the production of many isotopes becomes reduced when ^{22}Ne is fully concentrated at the center of the WD. The most affected, besides many neutron-rich isotopes of intermediate-mass elements, are: ^{50}Cr by an order of magnitude, ^{55}Mn and ^{53}Cr by a factor four, ^{54}Cr and ^{57}Fe by 60%, ^{51}V and ^{49}Ti by 40%, ^{58}Ni, ^{66}Zn, and ^{67}Zn by 25%, and so on. As in the sub-Chandrasekhar-mass WD models, the ^{40}Ca-to-^{32}S mass ratio increases in the full model by 30%,

[5] The density of the CNe shell is higher than that of the supporting CONe layer, meaning that, if it melts as a consequence of accretion, the CNe shell will progressively mix with inner layers.

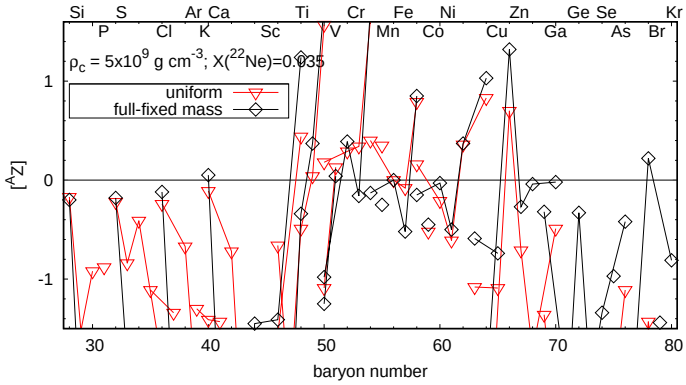

Fig. 7. Same as Fig. 6, but comparing the uniform composition model with case B for a WD of the same mass.

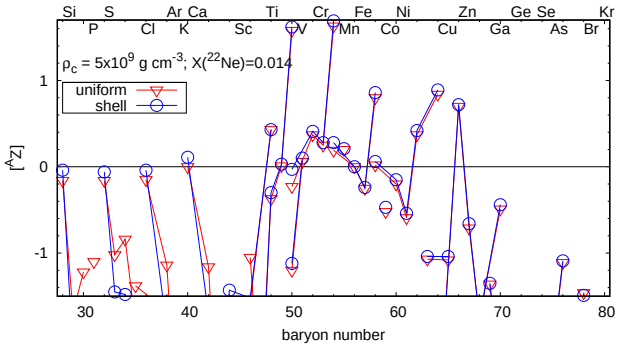

Fig. 8. Same as Fig. 6, but for the Chandrasekhar-mass models with $\rho_c = 5 \times 10^9$ g cm^{-3} and $Z = 0.014$.

with potential implications for the interpretation of X-ray spectra of SNe Ia remnants.

3.2.2. Influence of the conditions at thermal runaway on the final yields

The presence of ^{22}Ne in the central regions implies that, for a WD of the same mass, the central density has to be higher to reach hydrostatic equilibrium, and the importance of this effect increases when approaching the Chandrasekhar mass. Therefore, when comparing the effects of sedimentation with respect to the uniform model, one can choose to keep the central density fixed at thermal runaway, as in Fig. 6 and reported in the previous paragraphs, or to keep the WD mass constant, as in the sub-Chandrasekhar-mass scenario. As reported in Table 1, the full model with a mass equal to that of the uniform model has a central density of 6.9×10^9 g cm^{-3}. Still, the kinetic energy and ejected mass of ^{56}Ni are similar to those in the uniform model with a central density of 5.0×10^9 g cm^{-3}.

In Fig. 7, the yields of the uniform and full models with the same mass are compared. Due to the huge difference in central density at thermal runaway, the isotopic yields of both models are quite different. In the full model, selenium, germanium, gallium, zinc, and copper abundances increase from a factor of a few up to two orders of magnitude. On a more modest level, the synthesis of the most overproduced isotopes, ^{54}Cr and ^{50}Ti, is favored by the higher density of the full model, and their abundances increase by 36% and 67%, respectively, when compared to the uniform model. On the other hand, there are strong deficits of many isotopes of intermediate-mass elements, while the yields of ^{58}Ni, ^{54}Fe, and ^{55}Mn are reduced by factors two, three, and four, respectively.

3.2.3. Explosion after ^{22}Ne distillation in a solar-metallicity WD

Concerning the shell model, the impact on the nucleosynthesis of the Chandrasekhar-mass explosions is similar to that on the sub-Chandrasekhar-mass explosions, meaning that the quantitative impact is modest, except for some neutron-rich isotopes of intermediate-mass nuclei (Fig. 8). Among the few species whose yields are modified, the most important is ^{50}Cr, whose abundance rises by 42%, and ^{46}Ti, whose yield decreases by a factor three. Nevertheless, as can be seen in Table 1, it is noticeable that the yield of ^{56}Ni decreases by ∼10% when ^{22}Ne is concentrated in an off-center shell on a massive WD.

4. ^{56}Fe sedimentation: Scenarios and models

As mentioned in Sect. 1, an iron-enhanced solid phase can form thanks to the high atomic number of ^{56}Fe when the temperature is still too hot for a CO mixture to solidify. The solid can either be pure iron or a COFe alloy in which the iron number abundance is ∼15%; that is, an iron mass fraction of $X(^{56}\mathrm{Fe}) \sim 0.4$. In the case of pure iron, a solid ball of ∼0.001 solar masses forms in the center of a WD of solar metallicity. If the solid has the composition of the alloy, the size of the central region enriched in iron is 2.5 times larger (Camisassa et al. 2016).

As it is not possible to extract nuclear energy from iron, a pure iron ball does not favor the development of a thermonuclear SN explosion and it is necessary to explore the effects of different degrees of iron enrichment in the center of a WD. For these experiments, we used iron mass fractions from $X(^{56}\mathrm{Fe}) \sim 10^{-3}$ – which corresponds to a Solar System abundance of ^{56}Fe – to $X(^{56}\mathrm{Fe}) \sim 0.7$. The last value, and intermediate ones, are meant to represent either the COFe alloy mentioned earlier or an intermediate phase in the formation of the pure iron core at the center of a WD. In the models with $X(^{56}\mathrm{Fe}) > 10^{-3}$, that is all models but the homogeneous one, it is assumed that all iron is concentrated in a central ball, although the size of the ball changes as a function of the central value of $X(^{56}\mathrm{Fe})$, such that the total iron abundance in the WD remains the same in all cases.

4.1. Thermonuclear burning waves in COFe mixtures

As the properties of burning waves can be affected by the high abundances of iron assumed here, it is necessary to start exploring the feasibility of detonation waves and the structure and velocity of conductive flames in COFe mixtures. In the models reported in Sect. 4.2, a sub-Chandrasekhar-mass CO WD detonates as a consequence of a converging wave that ignites matter near the center of the star at a density of the order of a few times 10^7 g cm^{-3}. On the other hand, in the models reported in Sect. 4.3, conductive flames propagate through the center of a massive WD after experiencing a simmering phase, that is, during the first stages of the deflagrative phase of a delayed detonation, when the WD central density is of the order of $\rho_c = 5 \times 10^9$ g cm^{-3} (Piersanti et al. 2022). In the delayed detonation models, the detonation starts outside the zone enriched in iron.

4.1.1. Detonation

The study of the feasibility of a detonation in iron-rich matter follows a well-known procedure (e.g., Niemeyer & Woosley 1997)

consisting in solving the hydrodynamic and nuclear kinetic equations at (initial) constant density, with high spatial and temporal resolution. A homogeneous sphere made of a mixture of carbon, oxygen, and iron is endowed with a shallow temperature gradient at the center (the hot spot), such that shells burn one after the other in sequence and a pressure wave grows into the unburnt matter. If the hot spot is sufficiently large, the pressure wave transitions into a self-sustained detonation. The ^{56}Fe mass fraction has been given different values: $X(^{56}\mathrm{Fe}) = 0$, 0.35, 0.50, and 0.70, while both ^{12}C and ^{16}O mass fractions are equal to $0.5\left[1 - X(^{56}\mathrm{Fe})\right]$.

The code used in this study is the same hydrodynamic code used in the explosion models with gravitation turned off. In the present detonation calculations, the density is $\rho = 5\times10^{7}$ g cm^{-3} and the maximum temperature in the center of the detonating sphere is $T_{\max} = 3.2 \times 10^{9}$ K; except for the composition with $X(^{56}\mathrm{Fe}) = 0.70$, in which case it is $T_{\max} = 4 \times 10^{9}$ K. We also computed the minimum size of a hotspot able to detonate a COFe sphere with a lower maximum temperature of $T_{\max} = 2.8\times10^{9}$ K, and found no substantial variations in the results.

We find that, if the iron concentration stays below $X(^{56}\mathrm{Fe}) \simeq 0.5$, the size of the hot spot needed to start a detonation at $\rho = 5 \times 10^{7}$ g cm^{-3} lies between a few meters and 1 km, even though the precise values are somewhat dependent on the details of the thermal profile initially imprinted (Seitenzahl et al. 2009). As the radius of the iron-rich sphere in a solar-metallicity WD is 200−300 km, a detonation is a likely result even when half of the mass of the central sphere is iron.

However, if the iron abundance in the central sphere is as high as $X(^{56}\mathrm{Fe}) = 0.70$, a detonation is not obtained even for hot spot sizes as long as 1000 km, that is more than 3–4 times the size of the iron-rich region in a solar-metallicity WD, or more than 100 times its mass. Therefore, if the central iron mass fraction is high enough, a detonation can only be initiated outside the central iron-rich ball.

4.1.2. Conductive flame

As in the studies of detonating spheres, we determined the properties of conductive flames with different iron abundances by solving the hydrodynamic equations coupled to the nuclear kinetic equations with the same code used for the SN explosions with gravity turned off (such as the micro-zone hydrocode method described in Timmes & Woosley 1992). We computed the flame structure for $\rho = 5\times10^{9}$ g cm^{-3}, and at this density ^{56}Fe is unstable to a double electron capture. Therefore, all iron was transformed into ^{56}Cr before starting the hydrodynamic calculations. As in the previous section, we calculated the flame structure for different values of the ^{56}Cr mass fraction: $X(^{56}\mathrm{Cr}) = 0$, 0.35, 0.50, and 0.70, while both ^{12}C and ^{16}O mass fractions are equal to $0.5\left[1 - X(^{56}\mathrm{Cr})\right]$.

The flame velocity decreases with increasing ^{56}Cr abundance, from 140 km s^{-1} when $X(^{56}\mathrm{Cr}) = 0$ to 20 km s^{-1} when $X(^{56}\mathrm{Cr}) = 0.70$. At the assumed density, the size of the iron-rich ball in a solar-metallicity WD is of the order of 70 km, which means that it can be consumed by the flame in less than one second if the abundance of ^{56}Cr is $\lesssim$0.5 (flame velocity $\gtrsim$68 km s^{-1}).

The thermal and chemical structure of conductive flames at a density of 5×10^{9} g cm^{-3} are shown in Figs. 9 and 10 for two different cases, either matter initially composed of only ^{12}C and ^{16}O, or a mixture of both isotopes and ^{56}Cr, with $X(^{56}\mathrm{Cr}) = 0.50$. In the first case (top panel of Fig. 9), the chemical transmutation starts with the fusion reaction ^{12}C+^{12}C releasing both protons and alphas in almost equal numbers, together with ^{20}Ne and ^{23}Na, followed by ^{23}Na(p, α)^{20}Ne. Shortly after, the ^{20}Ne abundance decreases due to ^{20}Ne(α, p)^{23}Na and ^{20}Ne(p, α)^{17}O, and the α abundance equilibrates with those of ^{14}C, ^{17}O and neutrons, while the abundance of protons stabilizes through multiple reactions with intermediate-mass elements and carbon and oxygen isotopes. Thereafter, ^{28}Si and other intermediate-mass elements are synthesized following the oxygen-fusion reaction. Finally (top panel of Fig. 10), the abundance of ^{54}Fe increases and approaches its value at NSE.

In the second case (bottom panel of Fig. 9), the high initial abundance of ^{56}Cr is a trap for protons through the reaction ^{56}Cr(p, n)^{56}Mn, which prevents protons from contributing significantly to the building of intermediate-mass elements. In this case, there are never large amounts of the silicon or sulphur isotopes. Most species from the iron group are the result of (p, n) reactions with some contribution from (γ, n) disintegrations, while intermediate-mass elements are built on the basis of α-captures. Starting with a high abundance of ^{56}Cr is relatively efficient for achieving NSE, as can be seen when comparing the two panels in Fig. 10: the molar fractions of the most abundant isotopes change only slightly beyond $\sim2 \times 10^{-4}$ cm behind the flame front, while in the top panel a sizeable variation can be seen in the abundance of ^{28}Si after the front has advanced 10^{-3} cm. Despite the difference in efficiency, the width of the flame front (as defined by the destruction of both ^{12}C and ^{16}O) is greater in the second case than in the first case.

4.2. Sub-Chandrasekhar-mass detonation

In the following sections, we present our analysis of the nucleosynthesis resulting from the detonation of bare CO WDs of solar metallicity in which ^{56}Fe is concentrated in a central ball with different mass fractions. The models reported here adopt different values for the abundance of ^{56}Fe at the center of the WD: $X_{\rm c}(^{56}\mathrm{Fe}) = 10^{-3}$, which is roughly the Solar System fraction of ^{56}Fe and represents the case with no iron sedimentation at all; $X_{\rm c}(^{56}\mathrm{Fe}) = 0.35$, which is representative of the sedimentation of a COFe alloy as described by Caplan et al. (2021); and $X_{\rm c}(^{56}\mathrm{Fe}) = 0.50$ and 0.70, both cases belonging to an intermediate phase in the process of aggregation of a pure iron core. In all cases, the total mass of ^{56}Fe is the same and represents a fraction $X(^{56}\mathrm{Fe}) = 1.05 \times 10^{-3}$ of the WD mass. The metallicity is $Z = 0.014 = X(^{56}\mathrm{Fe}) + X(^{22}\mathrm{Ne})$ and the abundance of ^{22}Ne is homogeneous through the WD. Table 2 shows the models computed and the outcome of the explosion. As in the case of sedimentation of ^{22}Ne, the kinetic energy and the yield of ^{56}Ni are nearly insensitive to the sedimentation of ^{56}Fe.

Figure 11 shows the production factors of the sub-Chandrasekhar-mass models with different central concentrations of ^{56}Fe. Here, we see that the yield of every single isotope up to a baryon number $A = 70$ is unaffected by the separation of ^{56}Fe. Furthermore, the yields of the isotopes with $A > 70$ that are affected by this process are independent of the degree of concentration of ^{56}Fe in the center as long as it is absent from the WD mantle. The main changes in the nucleosynthesis are the reductions in the yields of selenium, gallium, germanium, krypton, and arsenic, which decrease down to a factor four, although the impact is uneven for the different isotopes of each element. Most of these species, in particular the p-nuclei ^{74}Se and ^{78}Kr, are synthesized during the explosion when the detonation front arrives at the outermost layers of the WD, approximately 0.03 $M_{\odot}$ below the surface, burning up to a temperature of 2.8−3.2 GK at a density of $\sim1-3 \times 10^{6}$ g cm^{-3} (a comprehensive description of the

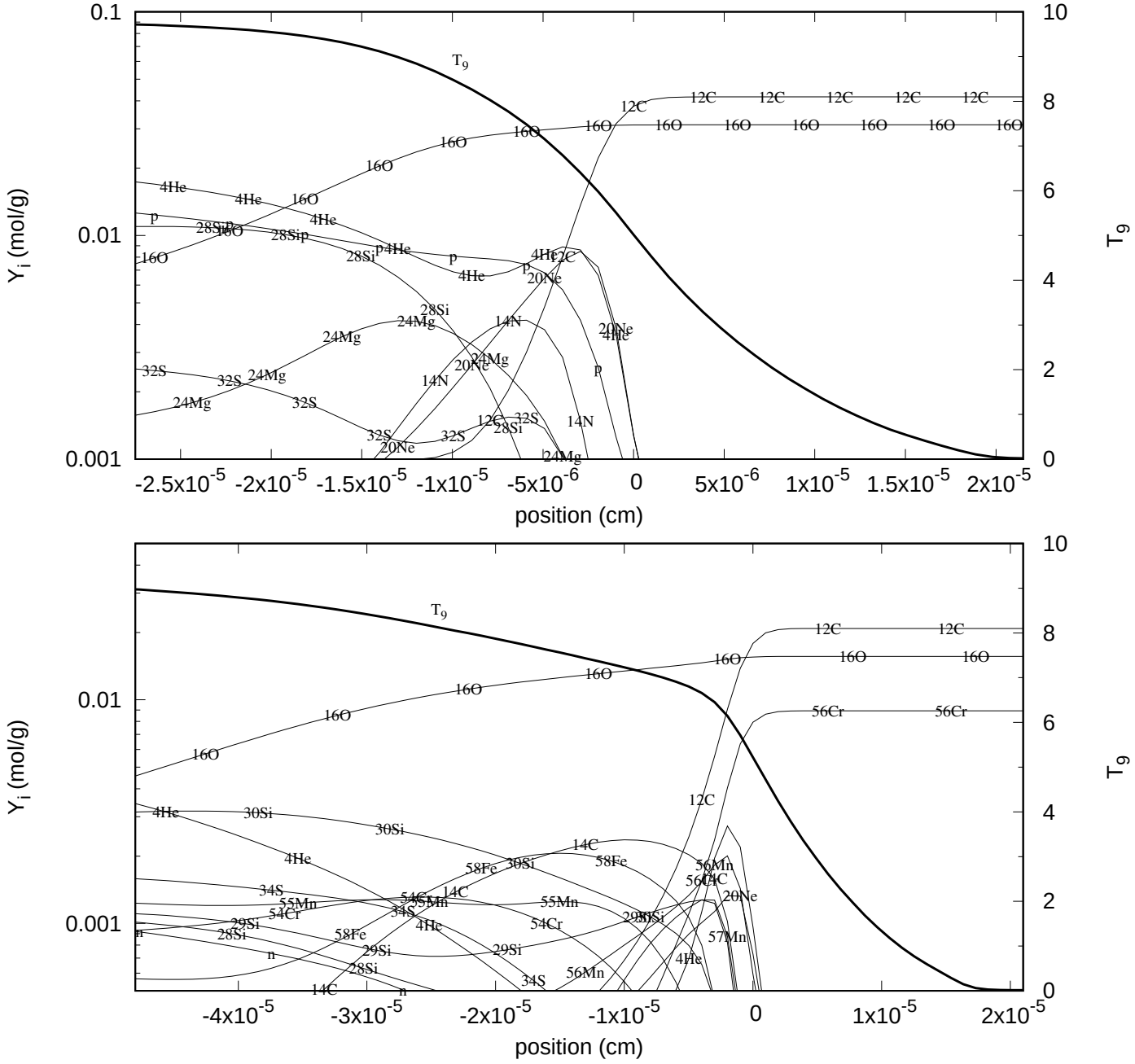

Fig. 9. Chemical structure of a conductive flame in 50%–50% ^{12}C–^{16}O (top) and 50%–25%–25% ^{56}Cr–^{12}C–^{16}O (bottom) mixtures at a density of 5×10^9 g cm^{-3}. The temperature is plotted with a thick line. The initial width of the shells was 10^{-6} cm.

p-process in SNe Ia can be found in e.g., Travaglio et al. 2011); they are the result of a γ-process starting from seed ^{56}Fe and are most affected by the migration of this isotope to the central layers of the WD.

4.3. Chandrasekhar-mass WD delayed detonation

Figure 12 shows the nucleosynthesis of the Chandrasekhar-mass models with a central density of $\rho_c = 3.5 \times 10^9$ g cm^{-3} and the different degrees of ^{56}Cr[6] concentration at the center detailed in Table 2. Two different trends can be identified in the plot concerning the changes induced by ^{56}Fe distillation. On the one hand, there are the $A > 70$ isotopes made on the external layers of the WD, the abundances of which drop sharply if iron is concentrated on the center of the WD, as in the sub-Chandrasekhar-mass scenario.

On the other hand, there are isotopes synthesized close to the center of the massive WD whose abundance is sensitive to the degree of concentration of ^{56}Cr in the central layers. Some examples are: ^{66}Zn, ^{64}Ni, ^{54}Cr, and ^{50}Ti, whose abundances are reduced by factors 2–7 with respect to the homogeneous model. The decrements in the abundances of these isotopes can be traced back to the small amount of nuclear energy released by burning ^{56}Cr. For instance, a mixture of 50%–25%–25% ^{56}Cr–^{12}C–^{16}O releases less than 60% energy than a mixture of 50%–50% ^{12}C–^{16}O. Less energy released means a lower temperature at NSE and a reduced capacity to create light nuclei,

[6] As explained in Sect. 4.1.2, all ^{56}Fe is converted to ^{56}Cr at the center of Chandrasekhar-mass WDs because of the high density.

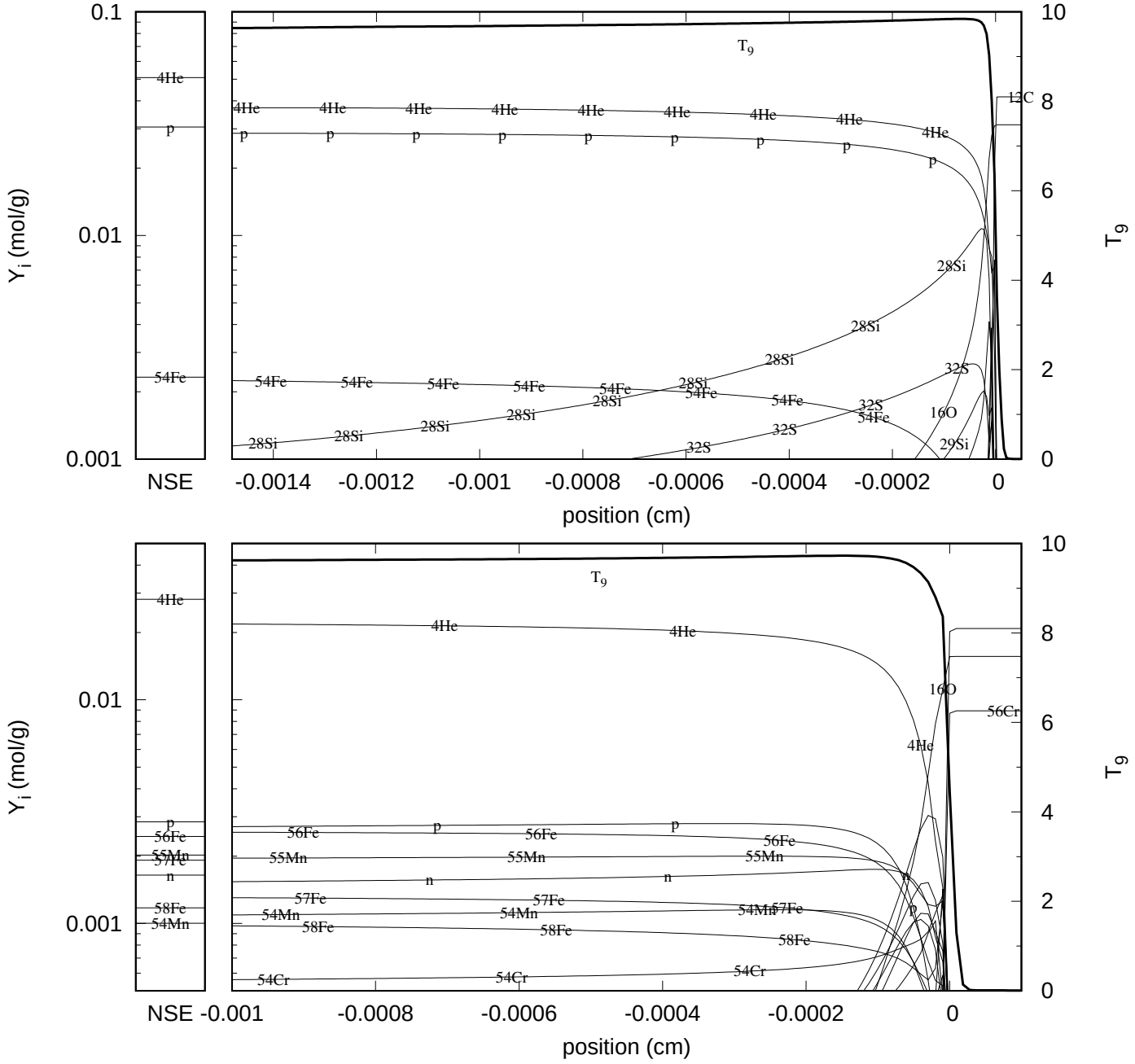

Fig. 10. Same as Fig. 9 but on a longer length scale. On the left, we show the molar abundances belonging to nuclear statistical equilibrium. For these flame simulations, the initial width of the shells was 5×10^{-6} cm (top) and 10^{-5} cm (bottom), while the respective electron mole numbers are 0.500 and 0.464 mol g^{-1}.

such as protons. As protons are the main contributors to neutronization by electron capture in NSE (Thielemann et al. 1986; Brachwitz et al. 2000), the final electron mole number is higher starting from the ^{56}Cr-contaminated mixture than when this species is absent.

We also examined whether the impact of ^{56}Fe sedimentation changes significantly with the central density of a massive WD by repeating the same models starting from $\rho_c = 5.0 \times 10^9$ g cm^{-3}, also summarized in Table 2. The results are almost the same as for $\rho_c = 3.5 \times 10^9$ g cm^{-3}, with the only relevant exception being the case of ^{48}Ca, which is strongly overproduced in the homogeneous model at the highest density and whose abundance suffers a decline of up to one order of magnitude if the explosion occurs after all ^{56}Fe has migrated to the center of the WD.

5. Explosion of a WD after distillation of ^{56}Fe and ^{22}Ne

As a final test, we explored the properties of the thermonuclear explosion of a stratified WD in which both ^{56}Fe and ^{22}Ne have migrated to the center forming a structure with three chemically differentiated zones. We built a 1.06 $M_\odot$ WD in hydrostatic equilibrium with a central ball containing all the ^{56}Fe of the WD[7], with a mass fraction of $X(^{56}\mathrm{Fe}) = 0.35$, surrounded by a shell composed of ^{12}C and the remaining ^{22}Ne with the

[7] The total mass of ^{56}Fe in the WD is 0.0027825 $M_\odot$, which is a fraction 2.625×10^{-3} of the WD mass, while the total mass of ^{22}Ne is 0.0371 $M_\odot$.

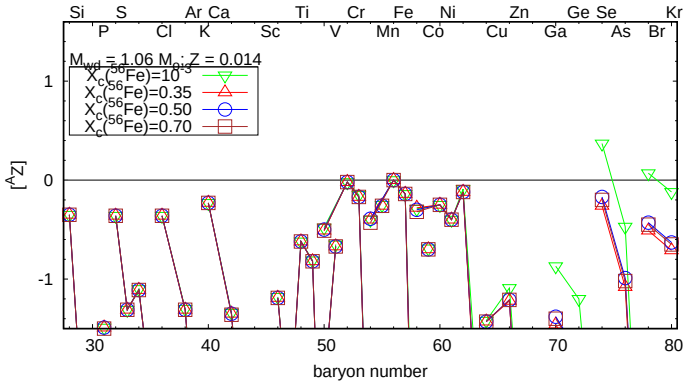

Fig. 11. Nucleosynthesis of sub-Chandrasekhar-mass bare CO detonation models with $M_{\rm WD} = 1.06\,M_\odot$ and $Z = 0.014$ with different central concentrations of ^{56}Fe (see Table 2 for details). The abundance of each isotope is given with reference to the final yield of ^{56}Fe and normalized to Solar System abundances, as in Fig. 2.

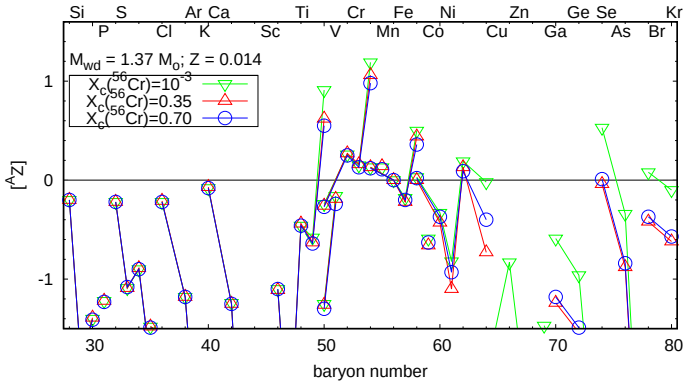

Fig. 12. Same as Fig. 11, but for the Chandrasekhar-mass delayed-detonation models with $\rho_{\rm c} = 3.5 \times 10^9$ g cm^{-3} and $Z = 0.014$.

azeotropic composition, that is $X(^{22}\mathrm{Ne}) = 0.30$, and finally a mantle made up of just ^{12}C and ^{16}O. The central density of this WD is $\rho_{\rm c} = 5.9 \times 10^7$ g cm^{-3}. We exploded a chemically homogeneous WD as well – with the same mass of each species as in the stratified model – to serve as a reference model[8]. This latter WD has a central density of $\rho_{\rm c} = 5.4 \times 10^7$ g cm^{-3}.

The results are shown in Table 3 and Fig. 13. A comparison with Tables 1 (uniform and full models in the first and third rows) and 2 (model with $X(^{56}\mathrm{Fe}) = 0.35$ in second row), and with Figs. 2 and 11 makes it clear that the impact of considering both ^{56}Fe and ^{22}Ne sedimentation is equivalent to the superposition of the effects of the sedimentation of each one independently. In spite of ^{56}Fe occupying the center of the WD and displacing the ^{22}Ne-rich region slightly outwards, in our models there is no distinguishable interference among the effects of their sedimentation on the nucleosynthesis result of a SNe Ia explosion.

6. Conclusions

We used a one-dimensional supernova code to explore the outcomes of thermonuclear explosions of frozen WDs in which some of the secondary (in terms of abundance) species separate upon crystallization and concentrate either on the center or on an off-center shell. To this end, a simple chemical profile was adopted at the beginning of the explosion, following the findings of the most recent studies of the phase diagram of carbon, oxygen, and impurities such as ^{22}Ne and ^{56}Fe. Complications such as remixing after solid melting or the composition of accreted matter were disregarded in order to discern what may be the maximum effect of chemical stratification on the properties of SNe Ia. The most relevant results concerning our models can be summarized as follows:

- Our models show that the chemical separation of ^{22}Ne and ^{56}Fe has a relatively limited impact on the main properties of SNe Ia, that is, their kinetic energy and ejected mass of ^{56}Ni.
- The sedimentation of ^{22}Ne with the azeotropic composition, $X(^{22}\mathrm{Ne}) = 0.30$, can leave an imprint on the SN yields. In sub-Chandrasekhar-mass explosions, the abundances of cobalt and copper increase and those of manganese and chromium decrease. In Chandrasekhar-mass explosions, the concentration of ^{22}Ne in the center of the WD harms the synthesis of most iron-group isotopes and, in particular, that of ^{55}Mn, which is reduced by a factor four.
- A high concentration of ^{22}Ne at the center of a Chandrasekhar-mass WD can affect the path to explosion, that is, the central density at thermal runaway, leading to decrements in the production of ^{58}Ni, ^{54}Fe, and ^{55}Mn of as much as factors of two, three, and four, respectively.
- The distillation of ^{56}Fe to the center of a WD hinders the synthesis of γ-process elements in the external layers, as is the case for ^{74}Se and ^{78}Kr.
- In Chandrasekhar-mass explosions, the yields of neutron-rich species such as ^{54}Cr can be strongly reduced, depending on the degree of concentration of ^{56}Cr (the by-product of double electron capture starting on ^{56}Fe) at the center at the time of explosion. However, the pre-explosive phase of accretion and simmering associated with Chandrasekhar-mass events has not been explored here. Therefore, we cannot discard the possibility that the low electron mole number of ^{56}Cr induces some kind of dynamical instability prior to the explosion and dilutes its concentration at the center of the WD.
- A self-sustained detonation is possible in iron-rich mixtures with carbon and oxygen at a density of 5×10^7 g cm^{-3} as long as the ^{56}Fe mass fraction in the mixture is lower than 0.7.
- Steady conductive flames can propagate through mixtures rich in iron-group elements at a density of 5×10^9 g cm^{-3}, even when the mass fractions of carbon and oxygen are as low as 0.15, although the flame velocity varies sharply with their initial abundance.
- The sedimentation of ^{22}Ne with the azeotropic composition has the potential of changing several signatures of progenitor metallicity (the ratio of calcium to sulphur) and of the character of the progenitor, whether a sub-Chandrasekhar-mass or a Chandrasekhar-mass WD (stable nickel profile and presence of a central hole in the distribution of radioactive nickel).

The degree of chemical separation depends on the time necessary to allow the WD to cool down to the solidification point, and an additional time, which can be quite long, to completely solidify. This means that, depending on the parameters of the explosion scenario, a variety a chemical structures can be at work. The main parameters defining the properties of the SN explosion seem not to be affected, but the use of minor species for diagnostic purposes has to be done with care and must be analyzed case by case.

In the case of ^{56}Fe sedimentation, the timescale is much shorter because the high atomic number of iron, as compared to

[8] The homogeneous WD differs from that in the first row of Table 1 because this latter does not include ^{56}Fe in the initial model.

Table 2. Summary of SNe Ia models with different central enhancements of ^{56}Fe (sub-Chandrasekhar-mass WDs) or ^{56}Cr (Chandrasekhar-mass WDs).

M_{WD} ($M_\odot$)	ρ_c (g cm^{-3})	$X_c(A=56)$ [a]	K (10^{51} ergs)	$M(^{56}Ni)$ ($M_\odot$)	$M(^{55}Mn)$ ($10^{-2}\,M_\odot$)	$M(^{58}Ni)$ ($10^{-2}\,M_\odot$)
Bare C-O WD detonations						
1.06	4.8×10^7	10^{-3}	1.319	0.655	0.410	1.35
1.06	5.0×10^7	0.35	1.324	0.656	0.402	1.39
1.06	5.1×10^7	0.50	1.324	0.656	0.399	1.34
1.06	5.2×10^7	0.70 [b]	1.323	0.656	0.395	1.27
Chandrasekhar-mass WD delayed detonations						
1.37	3.5×10^9	10^{-3}	1.410	0.669	1.05	3.08
1.37	3.5×10^9	0.35	1.418	0.671	1.07	2.87
1.37	3.5×10^9	0.70	1.421	0.675	1.01	2.97
1.38	5.0×10^9	10^{-3}	1.389	0.640	1.16	2.90
1.38	5.0×10^9	0.35	1.401	0.651	1.12	2.85
1.38	5.0×10^9	0.70	1.405	0.655	1.14	2.79

Notes. All models assumed a progenitor metallicity $Z = 0.014$. [a]Mass fraction of the stable isotope with $A = 56$ in the WD center: ^{56}Fe in sub-Chandrasekhar-mass WDs; ^{56}Cr in Chandrasekhar-mass WDs. [b]Ignition outside the central ball containing all ^{56}Fe.

Table 3. SNe Ia models after distillation of ^{56}Fe and ^{22}Ne.

Model	K (10^{51} ergs)	$M(^{56}Ni)$ ($M_\odot$)	$M(^{55}Mn)$ ($10^{-2}\,M_\odot$)	$M(^{58}Ni)$ ($10^{-2}\,M_\odot$)
Uniform	1.339	0.649	0.610	4.23
Stratified	1.338	0.633	0.257	6.62

Notes. All models assume a WD mass of $M_{WD} = 1.06\,M_\odot$ and a progenitor metallicity of $Z = 0.038$.

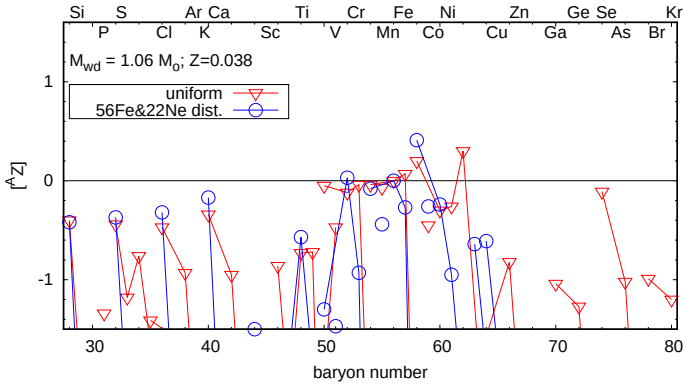

Fig. 13. Nucleosynthesis of sub-Chandrasekhar-mass bare CO detonation models with $M_{WD} = 1.06\,M_\odot$ and $Z = 0.038$, either with uniform chemical composition through the WD or chemically stratified after migration of ^{56}Fe and ^{22}Ne to the center of the WD. The abundance of each isotope is given with reference to the final yield of ^{56}Fe and normalized to Solar System abundances, as in Fig. 2.

carbon and oxygen, allows it to form a strongly coupled plasma at a relatively high temperature (Caplan et al. 2021). If iron and other high atomic number species present in a WD are able to migrate massively to the center before a SNe Ia explosion, the outer layers of the ejecta will lack any imprint of their initial metal content, except in the region containing the freshly accreted material. In normal-bright SNe Ia models assuming ^{56}Fe distillation, the abundance of iron and nickel (whose synthesis in the outer layers requires iron seeds) falls abruptly above ~20 000 km s^{-1}. As the presence of iron-group elements is expected to cause UV line blanketing and efficiently suppress the flux in this wavelength region (Lentz et al. 2000), the distillation of iron may affect the UV and cause the WD progenitor to be misinterpreted as a low-metallicity star. For the same reason, if the fraction of SNe Ia coming from frozen WDs is high enough, it may affect current attempts to establish a statistical correlation between the UV flux of these events and their host galaxy metallicity (Pan et al. 2020; Brown & Crumpler 2020).

Frozen chemically segregated WDs are expected to represent at most a fraction of the progenitors of SNe Ia. The delay time between the formation of a WD and a thermonuclear explosion is not constrained, but it can be in the range of a few tens of millions of years to several billion. If the time it takes a WD to start freezing is 1−3 Gyr, it can be estimated, applying the delay-time distribution of SNe Ia of Castrillo et al. (2021), that up to <20−40% of all SNe Ia can explode in a state of partial or total ^{22}Ne stratification and an even higher fraction may occur after ^{56}Fe sedimentation. Given the number of SNe Ia currently detected every year, it can be expected that many of these events occur in at least partially chemically segregated WDs. Therefore, it is important to keep in mind how this may affect the appearance of such events.

Acknowledgements. E.B. and L.P. acknowledge partial support from the Spanish grant PID2021-123110NB-100 funded by MCIN/AEI/10.13039/501100011033/FEDER/UE. J. I. acknowledges funding from MICIN/AEI grant PID2019-108709GBI00 and program Unidad de Excelencia Maria de Maetzu CEX2020-001058-M. L.P. acknowledges partial financial support from the Italian MUR project2022RJLWHN: Understanding R-process & Kilonovae Aspects (URKA).

References

Althaus, L. G., García-Berro, E., Renedo, I., et al. 2010, ApJ, 719, 612
Bildsten, L., & Hall, D. M. 2001, ApJ, 549, L219
Blondin, S., Bravo, E., Timmes, F. X., Dessart, L., & Hillier, D. J. 2022, A&A, 660, A96
Blouin, S., Daligault, J., Saumon, D., Bédard, A., & Brassard, P. 2020, A&A, 640, L11
Blouin, S., Daligault, J., & Saumon, D. 2021, ApJ, 911, L5
Brachwitz, F., Dean, D. J., Hix, W. R., et al. 2000, ApJ, 536, 934
Bravo, E., & Martínez-Pinedo, G. 2012, Phys. Rev. C, 85, 055805

Bravo, E., Isern, J., Canal, R., & Labay, J. 1992, A&A, 257, 534
Bravo, E., Althaus, L. G., García-Berro, E., & Domínguez, I. 2011, A&A, 526, A26
Bravo, E., Badenes, C., & Martínez-Rodríguez, H. 2019, MNRAS, 482, 4346
Brown, P. J., & Crumpler, N. R. 2020, ApJ, 890, 45
Camisassa, M. E., Althaus, L. G., Córsico, A. H., et al. 2016, ApJ, 823, 158
Caplan, M. E., Freeman, I. F., Horowitz, C. J., Cumming, A., & Bellinger, E. P. 2021, ApJ, 919, L12
Castrillo, A., Ascasibar, Y., Galbany, L., et al. 2021, MNRAS, 501, 3122
Caughlan, G. R., & Fowler, W. A. 1988, At. Data Nucl. Data Tables, 40, 283
Churazov, E., Sunyaev, R., Isern, J., et al. 2014, Nature, 512, 406
Churazov, E., Sunyaev, R., Isern, J., et al. 2015, ApJ, 812, 62
Cyburt, R. H., Amthor, A. M., Ferguson, R., et al. 2010, ApJS, 189, 240
De, S., Timmes, F. X., Brown, E. F., et al. 2014, ApJ, 787, 149
Deloye, C. J., & Bildsten, L. 2002, ApJ, 580, 1077
Diehl, R., Siegert, T., Hillebrandt, W., et al. 2014, Science, 345, 1162
Eitner, P., Bergemann, M., Hansen, C. J., et al. 2020, A&A, 635, A38
Fang, X., Thompson, T. A., & Hirata, C. M. 2018, MNRAS, 476, 4234
García-Berro, E., Althaus, L. G., Córsico, A. H., & Isern, J. 2008, ApJ, 677, 473
Hachisu, I., Kato, M., & Nomoto, K. 1999, ApJ, 522, 487
Hamers, A. S., & Thompson, T. A. 2019, ApJ, 882, 24
Han, Z., & Podsiadlowski, P. 2004, MNRAS, 350, 1301
Han, Z., & Podsiadlowski, P. 2008, in The Art of Modeling Stars in the 21st Century, eds. L. Deng, & K. L. Chan, 252, 349
Hernanz, M., Garcia-Berro, E., Isern, J., et al. 1994, ApJ, 434, 652
Höflich, P., Gerardy, C. L., Nomoto, K., et al. 2004, ApJ, 617, 1258
Horowitz, C. J., Schneider, A. S., & Berry, D. K. 2010, Phys. Rev. Lett., 104, 231101
Iben, I., Jr., & Tutukov, A. V. 1984, ApJS, 54, 335
Ichimaru, S., Iyetomi, H., & Ogata, S. 1988, ApJ, 334, L17
Isern, J., & Bravo, E. 2018a, Res. Notes Am. Astron. Soc., 2, 157
Isern, J., & Bravo, E. 2018b, arXiv e-prints [arXiv:1809.08789]
Isern, J., Hernanz, M., Mochkovitch, R., & Garcia-Berro, E. 1991, A&A, 241, L29
Isern, J., Mochkovitch, R., Garcia-Berro, E., & Hernanz, M. 1997, ApJ, 485, 308
Isern, J., García-Berro, E., Hernanz, M., Mochkovitch, R., & Torres, S. 1998, ApJ, 503, 239
Isern, J., García-Berro, E., Hernanz, M., & Chabrier, G. 2000, ApJ, 528, 397
Isern, J., Jean, P., Bravo, E., et al. 2016, A&A, 588, A67
Keegans, J. D., Pignatari, M., Stancliffe, R. J., et al. 2023, ApJS, 268, 8
Kushnir, D., Katz, B., Dong, S., Livne, E., & Fernández, R. 2013, ApJ, 778, L37
Lentz, E. J., Baron, E., Branch, D., Hauschildt, P. H., & Nugent, P. E. 2000, ApJ, 530, 966
Livne, E., & Arnett, D. 1995, ApJ, 452, 62
Lorén-Aguilar, P., Isern, J., & García-Berro, E. 2010, MNRAS, 406, 2749
Maoz, D., Mannucci, F., & Brandt, T. D. 2012, MNRAS, 426, 3282
Martínez-Rodríguez, H., Badenes, C., Yamaguchi, H., et al. 2017, ApJ, 843, 35
Mazzali, P. A., Sullivan, M., Filippenko, A. V., et al. 2015, MNRAS, 450, 2631
Medin, Z., & Cumming, A. 2010, Phys. Rev. E, 81, 036107
Mochkovitch, R. 1983, A&A, 122, 212
Niemeyer, J. C., & Woosley, S. E. 1997, ApJ, 475, 740
Nomoto, K. 1982a, ApJ, 257, 780
Nomoto, K. 1982b, ApJ, 253, 798
Nomoto, K., Thielemann, F. K., & Yokoi, K. 1984, ApJ, 286, 644
Ogata, S., Iyetomi, H., Ichimaru, S., & van Horn, H. M. 1993, Phys. Rev. E, 48, 1344
Pan, Y. C., Foley, R. J., Jones, D. O., Filippenko, A. V., & Kuin, N. P. M. 2020, MNRAS, 491, 5897
Piersanti, L., Bravo, E., Straniero, O., Cristallo, S., & Domínguez, I. 2022, ApJ, 926, 103
Renedo, I., Althaus, L. G., Miller Bertolami, M. M., et al. 2010, ApJ, 717, 183
Rosswog, S., Kasen, D., Guillochon, J., & Ramirez-Ruiz, E. 2009, ApJ, 705, L128
Salaris, M., Domínguez, I., García-Berro, E., et al. 1997, ApJ, 486, 413
Salaris, M., Cassisi, S., Pietrinferni, A., Kowalski, P. M., & Isern, J. 2010, ApJ, 716, 1241
Saumon, D., Blouin, S., & Tremblay, P.-E. 2022, Phys. Rep., 988, 1
Segretain, L. 1996, A&A, 310, 485
Segretain, L., Chabrier, G., Hernanz, M., et al. 1994, ApJ, 434, 641
Seitenzahl, I. R., Meakin, C. A., Townsley, D. M., Lamb, D. Q., & Truran, J. W. 2009, ApJ, 696, 515
Sim, S. A., Röpke, F. K., Hillebrandt, W., et al. 2010, ApJ, 714, L52
Thielemann, F.-K., Nomoto, K., & Yokoi, K. 1986, A&A, 158, 17
Timmes, F. X., & Woosley, S. E. 1992, ApJ, 396, 649
Travaglio, C., Röpke, F. K., Gallino, R., & Hillebrandt, W. 2011, ApJ, 739, 93
Webbink, R. F. 1984, ApJ, 277, 355
Whelan, J., & Iben, I., Jr. 1973, ApJ, 186, 1007
Woosley, S. E., & Kasen, D. 2011, ApJ, 734, 38
Woosley, S. E., & Weaver, T. A. 1994, ApJ, 423, 371
Xu, Z. W., & van Horn, H. M. 1992, ApJ, 387, 662